Bioactive Materials 43 (2025) 305–318

Contents lists available at ScienceDirect

Bioactive Materials

journal homepage: www.keaipublishing.com/en/journals/bioactive-materials

An intra articular injectable Mitocelle recovers dysfunctional mitochondria in cellular organelle disorders

Min Ju Lim [a,b,1], Hyeryeon Oh [c,d,1], Jimin Jeon [a], Chanmi Cho [a,e], Jin Sil Lee [c,f], Yiseul Hwang [b,g], Seok Jung Kim [h], Jung-Soon Mo [b,i], Panmo Son [c,j], Ho Chul Kang [b,g,***], Won Il Choi [c,**], Siyoung Yang [a,*]

[a] Department of Biological Sciences, Sungkyunkwan University, Suwon, 16419, Republic of Korea
[b] Department of Biomedical Sciences, Graduate School, Ajou University School of Medicine, Suwon, 16499, Republic of Korea
[c] Center for Bio-Healthcare Materials, Bio-Convergence Materials R&D Division, Korea Institute of Ceramic Engineering and Technology, 202, Osongsaengmyeong 1-ro, Osong-eup, Heungdeok-gu, Cheongju, Chungbuk, 28160, Republic of Korea
[d] School of Materials Science and Engineering, Gwangju Institute of Science and Technology, 123, Cheomdan-gwagiro, Buk-gu, Gwangju, 61005, Republic of Korea
[e] Center for Systems Biology, Massachusetts General Hospital Research Institute, Department of Radiology, Massachusetts General Hospital and Harvard Medical School, Boston, MA, 02114, USA
[f] Drug Manufacturing Center, Daegu-Gyeongbuk Medical Innovation Foundation (K-MEDI Hub), Daegu, 41061, Republic of Korea
[g] Department of Physiology, Ajou University School of Medicine, Suwon, Gyeonggi, 16499, Republic of Korea
[h] Department of Orthopedic Surgery, College of Medicine, The Catholic University of Korea, Seoul, 06591, Republic of Korea
[i] Institute of Medical Science, Ajou University School of Medicine, Suwon, 16499, Republic of Korea
[j] Department of Applied Bioengineering, Graduate School of Convergence Science and Technology, Seoul National University, Seoul, 08826, Republic of Korea

ARTICLE INFO

Keywords:
Mitocelle
Inhibition of NOX4-p22phox axis
Dysfunctional mitochondria
Cellular organelle disease
Arthritis

ABSTRACT

Mitochondrial dysfunction increases ROS production and is closely related to many degenerative cellular organelle diseases. The NOX4-p22phox axis is a major contributor to ROS production and its dysregulation is expected to disrupt mitochondrial function. However, the field lacks a competitive inhibitor of the NOX4-p22phox interaction. Here, we created a povidone micelle-based Prussian blue nanozyme that we named "Mitocelle" to target the NOX4-p22phox axis, and characterized its impact on the major degenerative cellular organelle disease, osteoarthritis (OA). Mitocelle is composed of FDA-approved and biocompatible materials, has a regular spherical shape, and is approximately 88 nm in diameter. Mitocelle competitively inhibits the NOX4-p22phox interaction, and its uptake by chondrocytes can protect against mitochondrial malfunction. Upon intra-articular injection to an OA mouse model, Mitocelle shows long-term stability, effective uptake into the cartilage matrix, and the ability to attenuate joint degradation. Collectively, our findings suggest that Mitocelle, which functions as a competitive inhibitor of NOX4-p22phox, may be suitable for translational research as a therapeutic for OA and cellular organelle diseases related to dysfunctional mitochondria.

1. Introduction

Mitochondrial activity is increasingly being acknowledged as contributing to both good health and various diseases [1]. Mitochondria are intracellular organelles that generate ATP and act as a critical hub for multiple pathology-related processes, including intracellular metabolism, calcium signaling, cell proliferation, and aging [2]. Of the reactive oxygen species (ROS) within cells, nearly 90 % is generated by mitochondria. Hence, mitochondrial malfunction leading to an imbalance between the creation and elimination of mitochondrial (mt) ROS

Peer review under responsibility of KeAi Communications Co., Ltd.
* Corresponding author. Department of Biological Sciences, Sungkyunkwan University, Suwon, 16419, Republic of Korea.
** Corresponding author. Center for Bio-Healthcare Materials, Bio-Convergence Materials R&D Division, Korea Institute of Ceramic Engineering and Technology, 202, Osongsaengmyeong 1-ro, Osong-eup, Heungdeok-gu, Cheongju, Chungbuk, 28160, Republic of Korea.
*** Corresponding author. Department of Biomedical Sciences, Graduate School, Ajou University School of Medicine, Suwon, 16499, Republic of Korea.
E-mail addresses: hckang@ajou.ac.kr (H.C. Kang), choi830509@kicet.re.kr (W.I. Choi), yangsy@skku.edu (S. Yang).
[1] These authors contributed equally to this paper.

https://doi.org/10.1016/j.bioactmat.2024.09.021
Received 22 April 2024; Received in revised form 18 August 2024; Accepted 17 September 2024

can lead to ROS overproduction [3]. This triggers oxidative stress [4] and subsequent mitochondrial failure, in a sequence of events that has been associated with aging, diabetes, cardiovascular disease, metabolic syndrome, cancer, Alzheimer's disease, degenerative joint disease, etc. [5–8]. Clearly, therefore, the enhancement of mitochondrial function could benefit a range of ailments.

Osteoarthritis (OA) is the predominant type of degenerative cellular organelle disorder [9]. In OA, mitochondrial dysfunction leading to increased ROS levels and decreased energy generation may contribute to inflammation, degradation of cartilage, and alterations in bone structure, such as the formation of osteophytes and changes in subchondral bone thickness [10]. Therefore, the pathological increase of ROS levels is a key factor in the initiation of OA pathology, and targeted interventions aimed at regulating mitochondrial dysfunction could potentially be used to treat OA. However, the existing therapeutic agents focus mainly on inhibiting cartilage inflammation and improving joint movement, such as through the use of cyclooxygenase-2 (COX2) inhibitors or hyaluronic acid (HA) injections [11,12].

NADPH oxidase (NOX), which is a primary generator of ROS, is located within the inner mitochondrial membrane [13]. Its primary variant, NOX4, contributes to producing ROS in several cell types by forming a complex with p22phox; in many degenerative cellular organelle disorders, NOX4 is over-expressed, leading to ROS imbalance and eventual mitochondrial malfunction [14–17]. In the development of OA, regulation of the NOX4-p22phox axis leads to ROS overproduction, which up-regulates various catabolic factors, such as matrix metalloproteinases (MMPs) and COX2 [18]. The literature suggests that OA onset is mediated via interleukin-1beta (IL-1β) whereas OA progression is linked to ROS. Moreover, an interplay between IL-1β and ROS intensifies the relevant inflammatory and catabolic mechanisms: IL-1β induces ROS generation, which triggers signaling pathways leading to IL-1β synthesis [19]. This establishes a self-sustaining loop of inflammation and oxidative stress in the joint. MMP up-regulation and COX2 activation are crucial factors in the development of joint injury. OA progression is expedited by MMP3 and MMP13, which are up-regulated by several catabolic pathways and play crucial roles in breaking down the extracellular matrix (ECM) components of cartilage [18]. Whereas COX2 primarily contributes to inflammation, the MMPs are ultimately responsible for the progressive ECM breakdown that leads to OA [19]. Effective management of OA may therefore be achieved by reducing ROS up-regulation to suppress catabolic factors.

A number of nanozymes with distinct enzyme-like capabilities have been developed to treat OA based on the generally accepted idea that suppressing ROS can mitigate free radical-induced cartilage damage and hinder inflammatory signaling [20]. For example, manganese dioxide (MnO_2) exhibits peroxidase-like behavior by breaking down H_2O_2 and reducing oxidative stress [21]. Cerium nanoparticles can counteract free radicals using diverse capabilities and powerful redox activity [22]. Prussian blue nanozymes (PB) are specifically recognized as biocompatible scavengers of ROS and have been approved by the United States Food and Drug Administration (US FDA) for clinical use. Zhang et al. reported that PB has multienzyme-like activities, including peroxidase, superoxide dismutase, and catalase activities [23]. In PB, a cubic structure is formed by divalent iron ions connected by cyanide bonds; this yields significant redox activity that can transform highly reactive substances (e.g., H_2O_2, oxygen, and hydroxyl radicals) into non-hazardous substances. The advantageous catalytic function of PB has been extensively examined in various ailments, including inflammatory OA, Alzheimer's disease, Parkinson's disease, pancreatitis, and colitis [24–26]. For successful use, PB must be stabilized with a suitable polymer template [27], or it will tend to accumulate and/or lose efficacy in physiological settings due to the intrinsic instability of metal-based nanozymes. Povidone is commonly utilized as a stabilizing polymer for PB complexes [25,28], and has received approval from the US FDA for use in biological applications. It can spontaneously form micelles and contains iron ion-binding molecules that facilitate its coordinated interaction and complexation with PB [29].

Here, we sought to develop mitochondria-targeting PB-based povidone micelles (designated "Mitocelle") as a nanotherapeutic that can scavenge ROS by inhibiting the NOX4-p22phox interaction. We employed multiple analytic methods to characterize Mitocelle, including ultraviolet–visible (UV–Vis) spectroscopy, dynamic light scattering (DLS), transmission electron microscopy (TEM), and x-ray diffraction (XRD) analyses. Nanozyme stability over a 2-week period was assessed in both an aqueous solution and a biological buffer, using a Zetasizer to measure the hydrodynamic diameter and polydispersity index (PDI). Biochemical and histological analyses were conducted both *in vitro* and *in vivo* to demonstrate that Mitocelle has efficacy in preventing OA development (Fig. 1A).

2. Materials and methods

2.1. Reagents

Povidone (molecular weight = 10 kDa), potassium ferricyanide, iron (II) chloride tetrahydrate, ethylenediaminetetraacetic acid (EDTA), phosphate-buffered solution (1 M, pH 7.4), 2-thiobarbituric acid (TBA), trichloroacetic acid (TCA), sodium hydroxide solution, *N*-(3-dimethylaminopropyl)-*N*-ethylcarbodiimide hydrochloride (EDC), and retinyl palmitate (RP, a vitamin A derivative) were purchased from Sigma-Aldrich (St. Louis, MO, USA). 2,2-Diphenyl-1-picrylhydrazyl (DPPH), iron (III) chloride, and 2-deoxy-D-ribose (99 %) were purchased from Alfa Aesar (Ward Hill, MA, USA). Hydrogen peroxide (30 %) and L-ascorbic acid were bought from Junsei Chemical Co. (Tokyo, Japan) and TCI (Tokyo, Japan), respectively. HyClone™ deionized water (DIW), HyClone™ phosphate-buffered saline (PBS), Cy5, and Cy5.5 mono NHS esters were bought from Cytiva (Marlborough, MA, USA).

2.2. Preparation and characterization of Mitocelle

Mitocelle was prepared using the double-precursor method, as reported previously [30]. Briefly, 3 mL of 75 mg/mL povidone solution was prepared in DIW and mixed with 1 mL potassium ferricyanide (5 mM) in DIW under magnetic stirring at 400 rpm for 30 min. Iron chloride tetrahydrate (1 mL; 5 mM) was slowly dropped into the reaction solution under magnetic stirring at 530 rpm. The mixture was stirred for 1 h and purified by centrifugation for 10 min at 738×*g* in an Amicon Ultra centrifugal filter (molecular cutoff 100 kDa; Merck Millipore, Billerica, MA, USA). As-prepared nanozymes were freeze-dried for 3 days and stored at −20 °C until use. The same procedure was used to prepare naked PB.

PB and Mitocelle were characterized using various analytic techniques. UV–Vis spectroscopy (Mega900, Scinco, Seoul, Republic of Korea) was used to obtain the UV–Vis absorption spectra of nanozymes. A Zetasizer (ELSZ-2000, Otsuka, Osaka, Japan) was used to determine the hydrodynamic diameters, zeta potentials, and PDIs of nanozymes. Their morphologies were observed using TEM (JEM-2100Plus HR, JEOL, Tokyo, Japan). XRD analysis was carried out using an x-ray diffractometer (Miniflex 600, Rigaku, Tokyo, Japan) to confirm the povidone coating of micelles. To assess stability, Mitocelle was stored for 2 weeks in DIW or PBS in a shaking incubator at 37 °C, and for 1 year in a lyophilized state at −20 °C. The diameters, PDIs, and zeta potentials were analyzed using a Zetasizer. The ROS-scavenging abilities of Mitocelle toward DPPH and hydroxyl radicals were evaluated as previously described [31,32]. Briefly, DPPH radical solution (0.5 mM) was prepared with methanol in the dark and reacted at a 1:1 volume ratio with various concentrations of Mitocelle (0.1, 0.5, 1, 5, and 10 mg/mL). The amount of active DPPH radicals was measured using a microplate reader at 515 nm. For the hydroxyl radical-scavenging assay, EDTA (0.1 mL, 0.1 mM), $FeCl_3$ (0.1 mL, 0.1 mM), deoxyribose (0.1 mL, 3.75 mM), H_2O_2 (0.1 mL, 1 mM), potassium phosphate buffer (0.5 mL, 20 mM), and ascorbic acid (0.1 mL, 0.1 mM) were mixed together and then combined

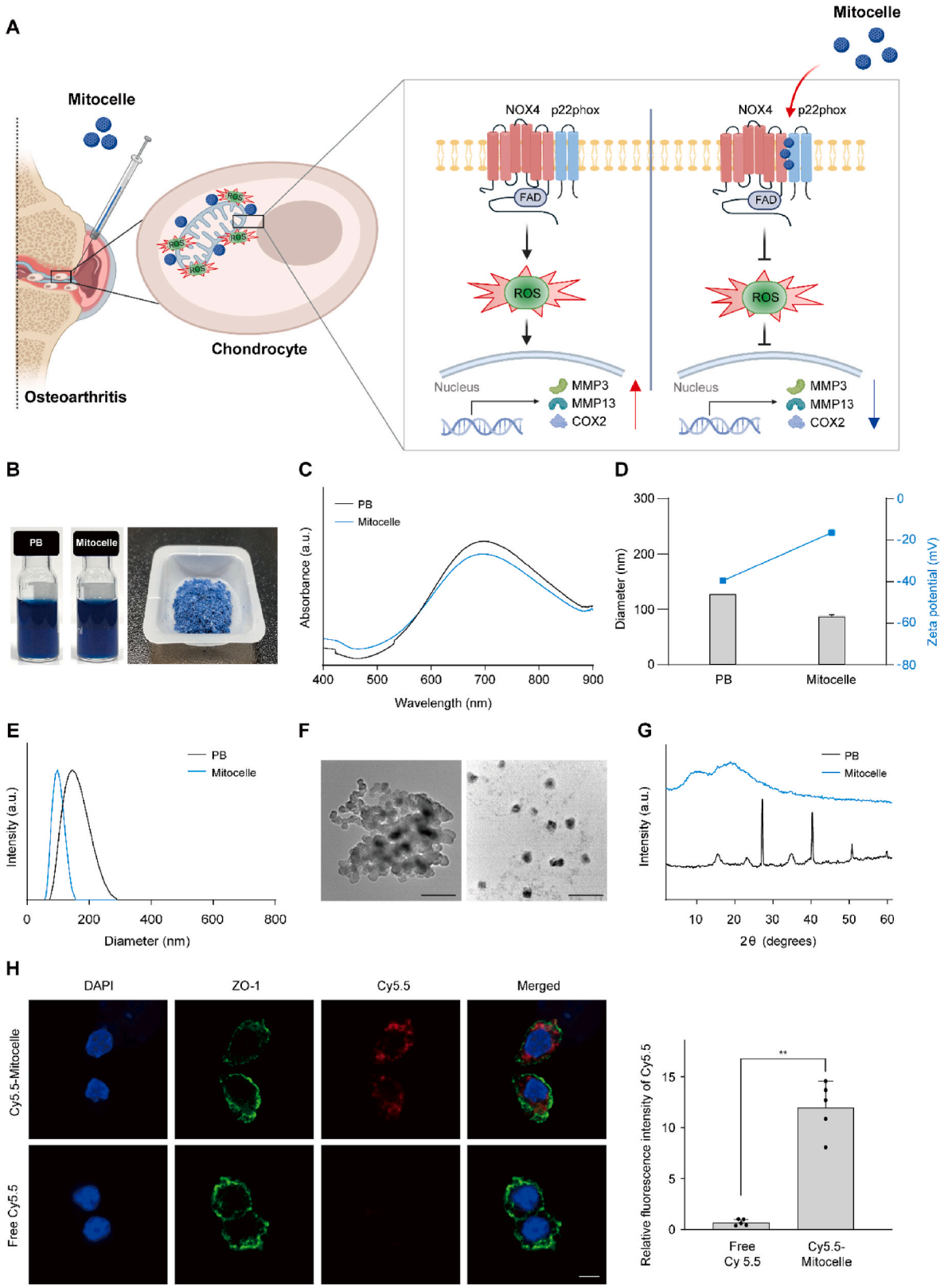

Fig. 1. Physicochemical properties of Mitocelle. (A) Schematic showing how Mitocelle can treat OA. (B) Photographs of dispersed and lyophilized Mitocelle. (C) Ultraviolet–visible absorption spectra, (D) hydrodynamic diameter and zeta potential, and (E) size distribution peaks of PB and Mitocelle. (F) Transmission electron microscopy images of PB (left) and Mitocelle (right). Scale bar, 500 nm. (G) X-ray diffraction spectra of PB and Mitocelle. (H) Immunofluorescence microscopy images of DAPI, ZO-1 (a membrane marker), and Cy5.5-labeled Mitocelle (left). Scale bar, 5 μm. Quantification of the fluorescence intensity of Cy5.5 (right). Data are presented as means ± SD ($n = 5$) and those in (H) were assessed using the Mann-Whitney U test. $^{**}P < 0.01$.

with 1 mL Mitocelle at various concentrations (0.1, 0.5, and 1 mg/mL). The reaction was carried out for 1 h in an incubator at 37 °C and terminated by heating the test solutions for 15 min at 85 °C with 1 mL TBA (1 % w/v in 50 mM NaOH) and 1 mL TCA (2 % w/v). Absorbance at 515 nm was measured using a microplate reader.

Mitocelle was labeled with the fluorescent dyes, Cy5.5 and Cy5, for our *in vivo* and protein microarray analyses, respectively. For Cy5.5 labeling, Mitocelle solution (50 mg/mL) was mixed with EDC (1 mg/mL) and Cy5.5 mono NHS ester (4 mg/mL) for 72 h at 25 °C. The unreacted dye was removed by centrifugation for 10 min at 738×*g* in an Amicon Ultra centrifugal filter and the properties of the labeled Mitocelle were analyzed using a microplate reader. The Cy5-labeled Mitocelle was prepared and analyzed as described above, except using 0.7 mg/mL EDC and 2.5 mg/mL Cy5 mono NHS ester.

2.3. Cell culture and viability assay

To obtain articular chondrocytes, cartilage was collected from 5-day-old ICR mice and digested with 0.2 % collagenase type II and 0.1 % trypsin as previously described [33]. The obtained chondrocytes were cultured in DMEM containing 10 % FBS, 100 units/mL of penicillin, and 100 μg/mL of streptomycin. To assess cytotoxicity, the isolated chondrocytes were cultured in 96-well plates (9×10^3 cells/well) for 3 days and treated with Mitocelle for 24 h. Supernatants were obtained and cell viability was measured using a lactate dehydrogenase (LDH) colorimetric assay kit (BioVision Inc., Milpitas, CA, USA). The LDH levels in media were normalized with respect to untreated (100 % viability) and Triton X-100-treated (0 % viability) samples and calculated by the formula: 100 – (sample LDH-negative control)/(maximum LDH-negative control) × 100. The absorbance of each well was measured at 495 nm using a SYNERGY H1 Microplate Reader (Biotek, Winooski, VT, USA).

2.4. RT-PCR and qRT-PCR

Total RNA of primary articular chondrocytes was extracted using TRIzol (Molecular Research Center, Cincinnati, OH, USA) and reverse-transcribed to cDNA (Intron Biotechnology, Republic of Korea). Relative gene expression was examined using quantitative reverse transcription-PCR (StepOnePlus Real-Time PCR System, Applied Biosystems, Foster City, CA, USA) and SYBR premix Ex Taq (TaKaRa Bio, Shiga, Japan). GAPDH was used for normalization to quantify relative gene expression [34]. The utilized primers are summarized in Table S1.

2.5. Measurement of PGE_2, collagenase activity, and intracellular ROS

Primary mouse articular chondrocytes were seeded to 96-well plates (2×10^4 cells/well), the culture media were collected, and the levels of PGE_2 were measured using a PGE_2 Immunoassay Kit (R&D Systems, Minneapolis, MN, USA) according to the manufacturer's protocol. For measurement of collagenase activity, the media were concentrated using Viva® Spin Columns (Sartorius Stedim Biotech, Göttingen, Germany), collagenase activity was assessed using an EnzChek™ Gelatinase/Collagenase Assay kit (e12055; Invitrogen, Carlsbad, CA, USA), and fluorescence signals were analyzed with a SYNERGY H1 microplate reader (BioTek Instruments, Winooski, VT, USA). Intracellular ROS levels were detected by DCF-DA fluorescent probe staining, as previously described [18]. In brief, chondrocytes were infected with Ad-NOX4 (800 MOI) for 2 h, treated with Mitocelle in fresh medium for 24 h, washed twice with PBS, and stained with 10 μM DCF-DA for 30 min at 37 °C. The cells were then analyzed by a flow cytometer (MACSQuant VYB, Miltenyi Biotec).

2.6. Protein isolation and Western blotting

Cells were lysed in RIPA lysis buffer (150 mM NaCl, 1 % NP-40, 50 mM Tris pH 8.0, 0.2 % sodium dodecyl sulfate [SDS], and 5 mM NaF) containing a phosphatase inhibitor cocktail and protease (Roche, Madison, WI, USA) and the obtained total proteins were quantified using a BCA protein assay kit (Thermo Scientific, Waltham, MA, USA). Equal amounts of protein were separated by 8–12 % SDS-PAGE and transferred to a polyvinylidene difluoride (PVDF) membrane. Total ERK was detected as a loading control. The antibodies used for Western blotting were as follows: anti-COX2 (SC-1745; Santa Cruz Biotechnology, Dallas, TX, USA), anti-MMP3 (ab52915; Abcam, Cambridge, UK), mouse anti-MMP13 (ab51072; Abcam, Cambridge, UK), and mouse anti-ERK (610408; Becton Dickinson, Bergen County, NJ, USA). Protein bands were detected using a secondary antibody and a SuperSignal West Dura kit (Thermo Fisher Scientific, Waltham, MA, USA). ERK was used as a housekeeping protein for subsequent analysis.

2.7. Protein microarray analysis

Protein microarray data were generated using the HuProt Human Proteome Microarray v3.1 (CDI Laboratories, Mayaguez, Puerto Rico), which contains more than 21,000 unique and individually purified full-length human protein clones. Briefly, the protein chip was equilibrated in microarray buffer (137 mM NaCl, 2.7 mM KCl, 4.3 mM Na_2HPO_4, 1.8 mM KH_2PO_4, pH 7.4, and 0.05 % Triton X-100) for 5 min at 25 °C and then incubated in blocking solution (5 % filtered skim milk in microarray buffer) for 1 h at 25 °C. To screen for proteins that bound to Mitocelle, the protein chip was washed three times (10 min per wash) with microarray buffer, incubated at 25 °C with free Cy5 or Cy5-Mitocelle (5 μg/mL) in PBS, and probed with anti-GST and an Alexa Fluor goat-anti-rabbit 546-conjugated secondary antibody (Invitrogen, Carlsbad, CA, USA). The protein chip was washed three times with microarray buffer, collected by centrifugation at 200×*g* for 2 min, and scanned using a GenePix 4000 B instrument (Molecular Devices, Sunnyvale, CA, USA). The signal-to-noise ratio (SNR) for each spot was obtained as the foreground-to-background signal normalized to the GST signal intensity.

2.8. Mitochondrial staining

To investigate mitochondrial movement and membrane potential, mitochondria were labeled with 100 nM MitoTracker ™ Green FM (Invitrogen) at 37 °C in the dark for 20 min, washed, and immediately imaged using a confocal laser scanning microscope (Cell discoverer7 with an LSM900; Carl Zeiss Microscopy GmbH, Jena, Germany) at the Three-Dimensional Immune System Imaging Core Facility of Ajou University. For visualization of mitochondrial membrane potential, chondrocytes were stained with 1 mg/mL JC-1 (Invitrogen) for 30 min at 37 °C and imaged under a confocal laser scanning microscope (A1R HD25 N-SIM S; Nikon Corporation, Minato, Tokyo) at the Three-Dimensional Immune System Imaging Core Facility of Ajou University.

2.9. Intracellular trafficking imaging

To assess the intracellular movement of Mitocelle, Cy5.5-Mitocelles were applied to chondrocytes for 24 h. The cells were incubated with 100 nM MitoTracker ™ Green FM for 30 min, harvested, fixed with 4 % PFA for 20 min, and permeabilized for 10 min in 0.5 % Triton X-100 in PBS at 25 °C. The cells were then blocked with 3 % BSA for 1 h, incubated overnight at 4 °C with primary antibodies against caveolin1 (3238) and Rab7 (9367; both from Cell Signaling, Danvers, MA, USA), and incubated for 1 h at 25 °C with Alexa fluor 568-conjugated secondary antibodies (A11011; Thermo Scientific, Waltham, MA, USA). Confocal images were obtained using an LSM900 microscope (Carl Zeiss Microscopy GmbH, Jena, Germany).

2.10. Fluorescence-based analysis of cartilage explants, chondrocytes, and cartilage

To assess the penetration depth of Mitocelle, explanted cartilage was exposed to free Cy5.5 and Cy5.5-labeled Mitocelle for 24 h and processed into 5-μm paraffin-embedded sections, and fluorescence was examined under an LSM980 NLO microscope (Carl Zeiss Microscopy GmbH, Jena, Germany). To determine the retention time of Mitocelle in the knee joint, 10-week-old C57BL/6 mice ($n = 3$) were intra-articularly injected with free Cy5.5 or Cy5.5-labeled Mitocelle (10 mg/kg) and retention times were assessed using an IVIS Spectrum (VISQUE InVivo Smart-LF, Vieworks). To examine internalization, chondrocytes were treated with Cy5.5-labeled Mitocelle and immunocytochemistry was performed. An antibody against the membrane marker, ZO-1 (clone ZO1-1A12; Invitrogen, Tokyo, Japan), was applied at 4 °C overnight, reacted with Donkey anti-Mouse IgG (H + L) Highly Cross-Adsorbed Secondary Antibody, Alexa Fluor Plus 488 (A-11029; Invitrogen) for 1 h, and observed with an LSM980 NLO microscope (Carl Zeiss Microscopy GmbH, Jena, Germany). To prepare cartilage samples, mice were given intra-articular injection of Cy5.5-labeled Mitocelle (10 mg/kg) or free Cy5.5 (amount equal to that of the Cy5.5-labeled Mitocelle group) using a Hamilton syringe (7635-01, Hamilton Company, Reno, NV, USA). Mouse knee joints were isolated, trimmed, and fixed in 4 % PFA, and cartilage was visualized. Images were obtained from the top of the cartilage using an LSM980 NLO system (Carl Zeiss Microscopy GmbH, Jena, Germany).

2.11. Spectrofluorometry and FRET microscopy

The plasmids encoding rat full-length NOX4 and rat full-length p22phox were as previously described [35]. The plasmids used in the fusion construct were mVenus-C1 (plasmid #27794) and mTurquoise2-N1 (plasmid #54843), and that used for the positive control fusion protein was pmVenus(L68V)-mTurquoise2 (plasmid #60493) (all from Addgene, Watertown, MA, USA). NOX4 was cloned into mVenus-C1 to add the Yellow Fluorescent Protein (YFP) tag, and p22phox was cloned into mTurquoise2-N1 to add the Cyan Fluorescent Protein (CFP) tag in the fluorescent fusion structures. Chondrocytes were seeded to 35-mm confocal dishes, transfected for 48 h with fluorescent fusion constructs encoding NOX4 or p22phox, washed with PBS, scraped, and subjected to protein quantification. FRET measurements were implemented by: (1) measuring sensitized emission, and (2) imaging via acceptor photobleaching. First, emission scans were collected using a CFP excitation wavelength of 434 nm to measure sensitized emission. To determine the effect of YFP fluorescence on emission at the CFP excitation wavelength, YFP fluorescence was subtracted from the emission curves of cells expressing both CFP and YFP. This curve was further normalized to the level of CFP fluorescence observed at 474 nm from cells expressing CFP alone.

To detect FRET via measurement of acceptor photobleaching, cells were prepared as described above and fixed with 4 % PFA. YFP, but not CFP, was bleached using an LSM900 microscope (Carl Zeiss). After five rounds of pre-bleaching, images were obtained and partially photobleached at 100 % laser power. The acquired data were analyzed using the Zen image software (Zeiss Zen 3.8). Non-bleached areas of the same cells were included as controls in the data analysis. The FRET images were normalized by applying a Gaussian filter and then obtained through ratio images using the physiology module. FRET efficiency was calculated with the following equation [36]:

$$FRET\ efficiency\ (E) = \frac{D_{post} - D_{pre}}{D_{post}} * 100$$

where D_{pre} and D_{post} are the donor intensities before and after photobleaching, respectively.

2.12. Gene set enrichment analysis (GSEA)

To explore the impact of Mitocelle on gene expression in NOX-overexpressing cells, GSEA (Molecular Signature Database, MSigDB) was performed on our RNA-seq data. The OA signature gene list was obtained from IPA analysis, and the OA signature genes were matched with the RNA-seq data and ranked by their change in expression between the conditions. GSEA, which was performed using the Broad Institute Java Desktop software (ver. 4.3) (www.broadinstitute.org/gsea), utilizes nonparametric Kolmogorov-Smirnov statistics to determine whether there is a significant expressional difference in the members of a specific gene set between the experimental and control groups [18].

2.13. Human OA cartilage and animals

Human OA cartilage was sourced from patients who underwent arthroplasty (Table S2). All patients provided written informed consent, and the collection was approved by the Institutional Review Board of the Catholic University of Korea (UC14CNSI0150). The undamaged portion of cartilage from human OA patients was defined as healthy cartilage. All animal experiments were approved by the Animal Care and Use Committee of Sungkyunkwan University (protocol code SKKUIACUC2023-07-17-1). Mice (male C57BL/6 and ICR) weighing 18–20 g were purchased from DBL (Chungcheongbuk-do, Republic of Korea). C57BL/6J-background homozygous NOX4-KO mice ($NOX4^{-/-}$) were purchased from Jackson Laboratory (Bar Harbor, Maine, USA).

2.14. DMM-induced mouse model of OA and intra-articular injection

We established an OA model by performing destabilization of the medial meniscus (DMM) surgery in 12-week-old male C57BL/6 mice according to a previously described protocol [37]. Beginning at 4 weeks after DMM surgery, PBS or Mitocelle (50 mg/kg) were injected at intervals of 1, 2, and 4 weeks via intra-articular injection. Mouse knee joints were processed for histological analysis at 10 weeks after surgery.

2.15. Histology and immunohistochemistry

Collected mouse knee joints were decalcified in 0.5 M EDTA (pH 7.4) for 2 weeks. Human OA cartilage and decalcified mouse knee joints were trimmed, embedded in paraffin, and sectioned at 5 μm. The sectioned samples were subjected to Safranin-O staining, Alcian blue staining, or immunostaining. Additionally, a tidemark representing the interface between calcified and non-calcified cartilage within the joint is shown to illustrate degenerative changes in the articular cartilage. Cartilage destruction was scored using the OARSI (Osteoarthritis Research Society International) grading system (grade 0–6) [18], and osteophyte formation, SBP thickness, and synovitis scores were measured as previously described [38]. Immunohistochemical staining was performed overnight at 4 °C with primary antibodies against NOX4, MMP3, MMP13 (all from Abcam, Cambridge, UK), and COX2 (Proteintech, Rosemont, IL, USA). An appropriate secondary antibody was applied for 1 h at 25 °C, and protein expression was detected using AEC + high-sensitivity ready-to-use substrate chromogen (Dako, Santa Clara, CA, USA). Sections were viewed using a Nikon Eclipse Ni microscope (Tokyo, Japan). For histopathological analysis, lung, liver, and kidney tissues were fixed in 4 % paraformaldehyde, embedded in paraffin, stained with hematoxylin for 3 min, and stained with eosin for 10 min. Infiltration was scored as: 0 = normal, 0.5 = trace, 1 = mild, 2 = moderate, 3 = severe lymphocytic, and 4 = complete destruction. Two independent investigators performed blind scoring of all histopathology samples.

2.16. In vivo biodistribution assay

To examine the biodistribution of Mitocelle *in vivo*, free Cy5.5 and Cy5.5-Mitocelle (10 mg/kg) were intra-articularly injected into the

knees of 10-week-old male C57BL/6 mice. *In vivo* imaging of mice was performed at 12, 24, 48, 72, 96, 120, and 168 h post-injection. To measure fluorescence intensity within major organs and joints, mice were euthanized, and the heart, lungs, liver, spleen, kidney, and knee were excised and imaged (exposure time, 1 s) using an IVIS Spectrum (VISQUE InVivo Smart-LF, Vieworks [Anyang-si, Republic of Korea]).

2.17. Statistical analysis

All experiments were performed more than three times. Data are presented as the means ± standard deviation (SD). Differences between groups were compared using the Mann-Whitney *U* test and one-way ANOVA with Bonferroni's test. For non-parametric data, two groups were analyzed using the Mann-Whitney *U* test. Statistical analyses were performed using the GraphPad Prism 9 software (GraphPad Software, San Diego, CA, USA). *P*-values < 0.05 were considered to indicate statistical significance.

3. Results

3.1. Design and characterization of Mitocelle

Mitocelle was prepared by performing metal intercalation of iron cations on povidone without any reducing agent: The iron cations became electrostatically bound to the negatively charged oxygen atoms on the heterocycles of povidone, thereby enabling the nucleation of PB (Fig. S1A). In contrast to the previously reported strategies involving PB [39], our method does not require any harsh and/or acidic condition, such as the use of high temperature, ultrasonication, and/or hydrochloric acid. The formation of cyanide-bridged iron (II)-iron (III) complexes in the mixture of PB and Mitocelle was signaled by the appearance of blue coloration. As-prepared nanozymes could be lyophilized into a powder for storage and transportation (Fig. 1B). A UV–Vis absorption peak typical of the Fe (II)-CN-Fe (III) bond was observed at approximately 700 nm in the spectra of both PB and Mitocelle (Fig. 1C). DLS analysis revealed that the hydrodynamic diameters of PB and Mitocelle were 129 ± 1 nm and 88 ± 2 nm, respectively (Fig. 1D). We speculate that the metal-agglomerated PB exhibited a size reduction upon povidone coating due to the stabilizing effect of povidone. The zeta potential of PB was −39.5 ± 1 mV while that of Mitocelle was −16.4 ± 1 mV, reflecting the surface coating of PB with povidone, which has a less negative charge (Fig. 1D). Mitocelle had a narrow size distribution, indicating that monodispersed nanozymes had been formed (Fig. 1E). The PDIs of PB and Mitocelle were 0.25 ± 0.01 and 0.23 ± 0.03, respectively. TEM-based assessment of morphology revealed that Mitocelle was spherical and uniform in size (Fig. 1F right), whereas PB formed large and irregular agglomerates, reflecting its instability (Fig. 1F left). The XRD curve (Fig. 1G) confirmed the presence of a povidone coating in Mitocelle: The characteristic peaks of PB at $2\theta = 17.3°$, 24.5°, 35.2°, 39.5°, and 43.3° were hidden by the amorphous peak of povidone, verifying that the nanozymes had been encapsulated by the polymer template [40]. To assess the stability of Mitocelle, we monitored its size and PDI during storage in an aqueous solution and a biological buffer (Figs. S1B and C). Naked PB underwent aggregation directly after being dispersed in PBS. In contrast, Mitocelle remained stable for 2 weeks, without forming any partial aggregate. The initial diameters of Mitocelle in DIW and PBS were, respectively, 98 ± 13 nm and 151 ± 20 nm at the beginning of storage and around 92 ± 1 nm and 132 ± 45 nm after 2 weeks. The PDIs of Mitocelle were below 0.3, indicating that the size distribution remained uniform under storage. The zeta potential of Mitocelle was −19.6 ± 1 mV after 2 weeks of storage at 37 °C, indicating that the electrostatic repulsion of Mitocelle, and thus its stability, was maintained (Fig. S1D). The long-term stability of Mitocelle was analyzed after 2 weeks of storage in an aqueous solution and 1 year of storage in the lyophilized state, and the results revealed that Mitocelle retained its physicochemical properties under long-term storage (Fig. S1E−**G**). These results indicate that, compared to PB, Mitocelle exhibits an enhanced stability that should facilitate its biomedical application. Mitocelle also exhibited prominent and dose-dependent DPPH and hydroxyl radical-scavenging activities. The DPPH radical scavenging activity of 10 mg/mL Mitocelle was 36.5 % (Fig. S1H). Mitocelle exhibited a very stronger hydroxyl radical scavenging activity against DPPH radicals, likely reflecting the reported ability of PB to preferentially bind hydroxyl radicals [41]. The antioxidant activity of Mitocelle in neutralizing hydroxyl radicals increased dose-dependently from 35.0 % at 0.1 mg/mL to 86.4 % at 1 mg/mL (Fig. S1I). To examine the biological role of Mitocelle in chondrocytes, we used Cy5.5 labeling. Our analyses revealed that this labeling did not affect the physiochemical properties of Mitocelle, as evidenced by the lack of change in the UV–Vis absorption spectra (Fig. S2). We also found that Mitocelle was internalized into the cytoplasm and did not appear to exert cellular cytotoxicity (Fig. 1H, and Fig. S3). Based on previous reports on the cellular trafficking pathway between endosomes and mitochondria [42], the involvements of caveolin 1 and Rab7 in membrane trafficking and endosomal function [43,44], and the requirement for these proteins at the mitochondria-endosome interaction site [45–47], we used caveolin 1 and Rab7 as markers to further examine the Mitocelle internalization pathway. Indeed, our confocal microscopic analysis demonstrated that, upon cellular up-take, Mitocelle became fused to endosomal membranes positive for caveolin 1 and Rab7, and subsequently underwent translocation to mitochondria (Fig. S4).

3.2. Mitocelle targets NOX4 to regulate dysfunctional mitochondria

To characterize the impact of Mitocelle in the cytosol, we used the HuProt™ 3.1 human proteome microarray, which contains more than 21,000 human proteins. We confirmed through UV–Vis absorption and fluorescence spectra that Cy5 labeling of Mitocelle did not alter the absorbance or fluorescent properties of the components (Fig. S5). The results were obtained by exposing the protein array to anti-GST and an appropriate Alexa Fluor 546-conjugated goat-anti-rabbit secondary antibody (Fig. 2A and B). Along with the proteome microarray data, we analyzed a list of intracellular organelle-related proteins extracted from IPA. Our results confirmed that Mitocelle has high binding affinity for mitochondria-related proteins. Among them, we verified that NOX4 (SNR > 1.0) is a direct interaction partner of Mitocelle (Fig. 2C, Fig. S6). NOX4 overexpression leads to mitochondrial dysfunction in various cellular diseases [48] and NOX4 is responsible for producing H_2O_2 as a key signaling molecule for catabolic factor expression in OA [49].

Next, we monitored the movement of Mitocelle in chondrocytes in which mitochondria had been damaged by H_2O_2 treatment or NOX4 overexpression. Real-time live imaging analysis showed that Mitocelle exhibited Brownian motion independent of mitochondrial movement under normal conditions, whereas it tracked dysfunctional mitochondria in H_2O_2-treated and Ad-NOX4-infected chondrocytes (Fig. 2D, Fig. S7). We then evaluated whether mitochondrial dysfunction induced by NOX4 could be restored by Mitocelle. Mitochondrial membrane potential is a critical physiological parameter that reflects the health and function of mitochondria. A decrease in the mitochondrial membrane potential of NOX4-overexpressing cells is usually indicative of mitochondrial dysfunction [17]. JC-1 is a fluorescent dye that can reflect mitochondrial membrane potential by forming aggregates in the mitochondrial matrix under high membrane potential or monomers under low membrane potential [50]. We found that the fluorescence intensity of JC-1 aggregates was greatly reduced in Ad-NOX4-infected chondrocytes, indicating that the mitochondrial membrane potential was decreased in these cells. Importantly, however, this was dose-dependently restored by Mitocelle treatment (Fig. 2E). Together, our findings indicate that Mitocelle tracks defective mitochondria in NOX4-overexpressing chondrocytes and restores chondrocyte health by interacting with NOX4 to rescue the mitochondrial membrane potential.

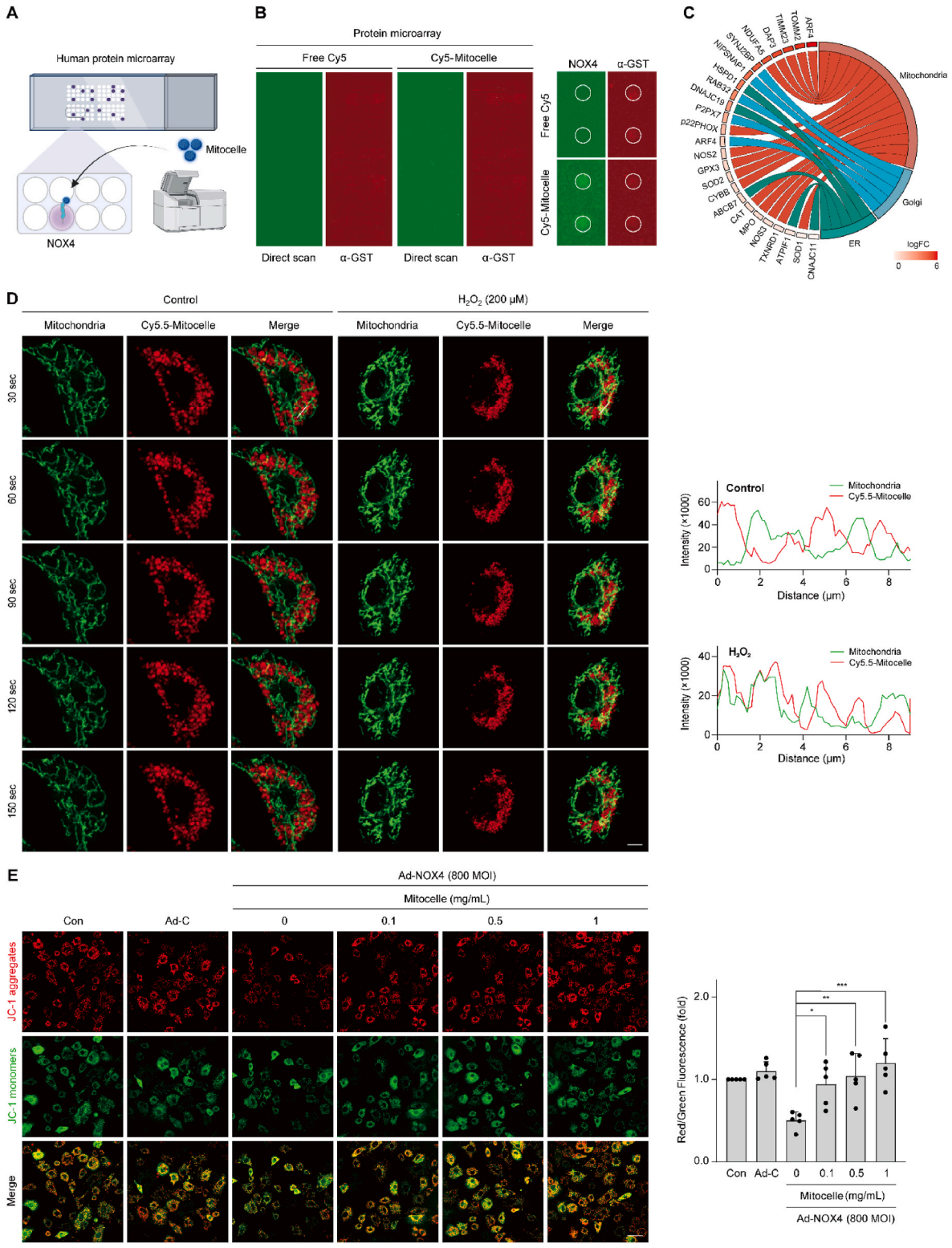

Fig. 2. Mitocelle can track and bind stressed mitochondria. (A) Schematic diagram of the human protein microarray analysis. (B) Mitocelle-interacting proteins were analyzed using the HuProt™ 3.1 human protein chip. The signal-to-noise ratio (SNR) for each spot was calculated as the ratio of the foreground-to-background signal. In addition, the GST signal intensity (red) was used for SNR normalization (left). A high-power image of NOX4 binding (white circles) is shown in the right panel. (C) Chord diagram visualizing the relationship between proteins with SNR > 1.0 and a list of mitochondrial, Golgi, and ER proteins. The SNR was calculated using the formula SNR $= 20 \log_{10}$ (Is In^{-1}), where 'Is' indicates the signal and 'In' indicates the noise. (D) Mouse chondrocytes treated with and without H_2O_2 were analyzed by real-time live imaging of mitochondria (green) and Mitocelle (red) using a Celldiscoverer7 and an LSM900 confocal microscope. Intensity profiles of linear regions of interest are shown in the right panel. (E) To confirm mitochondrial dysfunction, we performed JC-1 staining and quantified JC-1 aggregates (red) and JC-1 monomers (green) as average intensities expressed in arbitrary units. Data are presented as means ± SD ($n = 5$) and were assessed using one-way ANOVA with Bonferroni's test. $^{*}P < 0.05$, $^{**}P < 0.01$, $^{***}P < 0.001$.

3.3. Depletion of NOX4 protects against OA development

NOX4 has been implicated in the regulation of cartilage homeostasis and the function of chondrocytes, which are the cells responsible for producing and maintaining cartilage. Studies have indicated that NOX4-derived ROS may play roles in cartilage development and the responses to cartilage destruction and inflammation [18]. To characterize the function of NOX4 in OA, we first assessed its expression in OA cartilage. We observed that NOX4 expression was increased in damaged regions of human and mouse OA cartilage (Fig. 3A and B). To examine whether NOX4 overexpression was correlated with OA pathogenesis, we performed *in silico* analysis of RNA-seq data obtained from NOX4-encoding adenovirus (Ad-NOX4)-infected versus control chondrocytes. Gene set enrichment analysis (GSEA) demonstrated that Ad-NOX4-infected chondrocytes were strongly enriched for the OA gene signature (Fig. 3C). We selected several genes functionally related to matrix degradation, inflammation, and ROS production, and confirmed that their protein levels were also up-regulated (Fig. 3D and E). We also

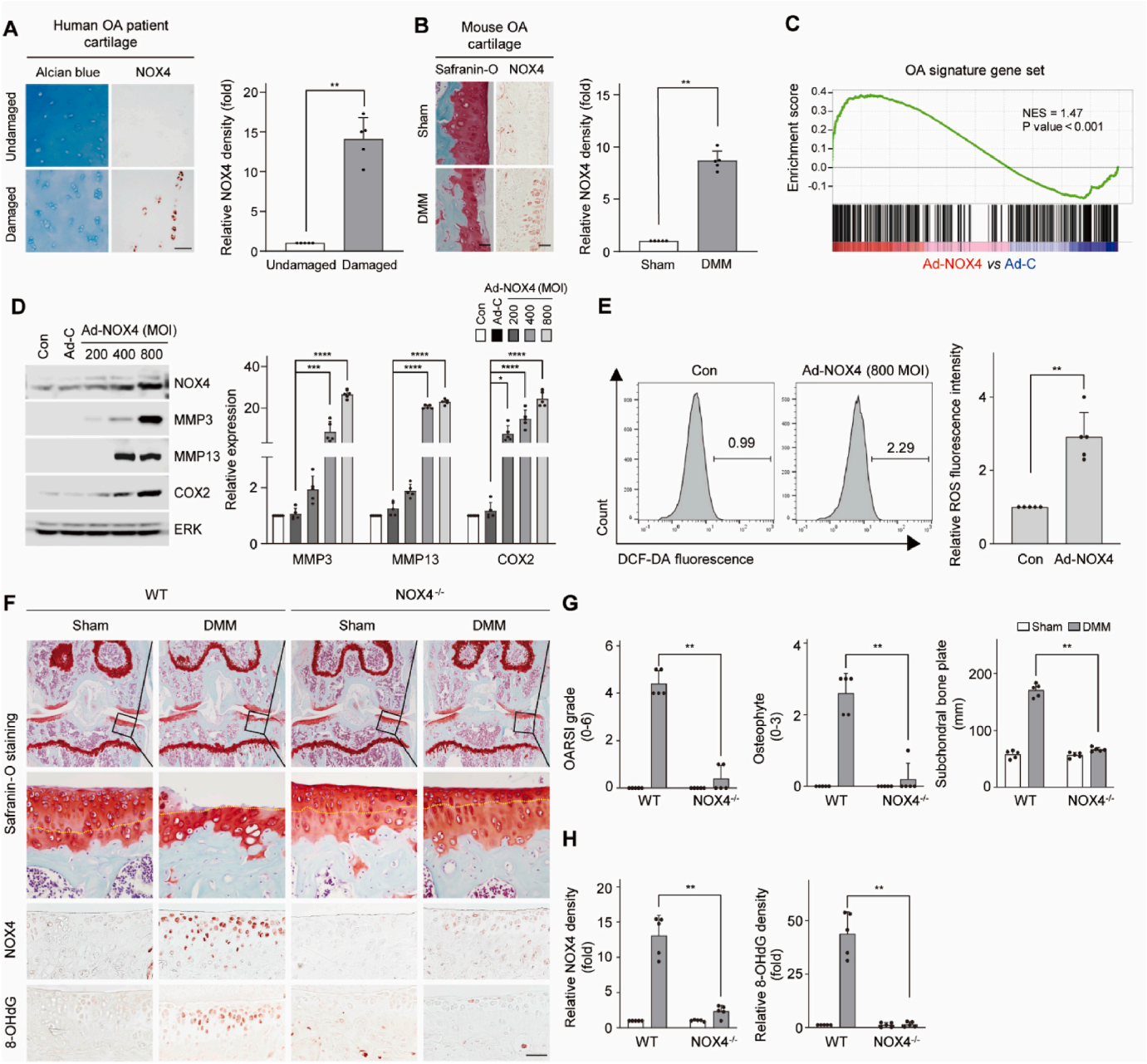

Fig. 3. NOX4 expression is altered in osteoarthritis (OA). (A) NOX4 expression in human OA patient cartilage (left) and relative densitometry (right). Scale bar, 100 μm. (B) Expression of NOX4 in cartilage from mice with DMM-induced OA (left) and relative densitometry (right). Scale bar, 100 μm. (C) Gene set enrichment analysis (GSEA) of signature genes in chondrocytes infected with Ad-C or Ad-NOX4. (D) Expression levels of NOX4, MMP3, MMP13, and COX2 proteins in Ad-NOX4-infected chondrocytes, as detected by Western blot analysis (left) and analyzed by relative densitometry (right). (E) Intracellular ROS levels measured using DCF-DA in chondrocytes infected with Ad-NOX4 (800 MOI). (F) Safranin-O staining and immunohistochemistry of NOX4 and 8-OHdG (ROS marker) in DMM-induced cartilage of wild-type and NOX4$^{-/-}$ mice. Scale bar, 100 μm. (G) Cartilage degradation was evaluated by OASRI score, osteophyte formation, and subchondral bone plate thickness (SBP). (H) Relative density of NOX4 and 8-OHdG signals in DMM-induced cartilage of wild-type and NOX4$^{-/-}$ mice. Yellow dotted lines indicate tidemarks (F). Data are presented as means ± SD ($n = 5$) and were assessed using (A, B, E, G, H) Mann-Whitney *U* test or (D) one-way ANOVA with Bonferroni's test. $^{*}P < 0.05$, $^{**}P < 0.01$, $^{***}P < 0.001$, $^{****}P < 0.0001$.

verified that the mRNA expression levels of OA catabolic factors were increased by NOX4 (Fig. S8). Next, we examined the phenotype of NOX4-depleted mice in which OA development was triggered by destabilization of the medial meniscus (DMM) surgery. As expected, NOX4-knockout ($NOX4^{-/-}$) mice exhibited decreased osteoarthritic cartilage destruction (Fig. 3F). Furthermore, OA manifestations, such as cartilage destruction, osteophyte formation, and subchondral bone sclerosis, were significantly decreased in DMM-induced $NOX4^{-/-}$ mice, as were catabolic factor levels and ROS production (Fig. 3G and H). Based on the above results, we hypothesize that the interaction of Mitocelle and NOX4 may inhibit NOX4-mediated ROS production and OA-related catabolic factor expression, suggesting that this novel nanozyme could potentially be suitable for OA therapy.

3.4. Penetration and retention of Mitocelle in mouse cartilage

Localized delivery of nanoparticles with extended retention in the joint is an excellent strategy for targeting the site of OA development and potentially eliminating the need for repeated injections. To monitor the penetration of Mitocelle into the cartilage matrix, *ex vivo* explanted cartilage from mouse joints was exposed to Cy5.5-Mitocelle or free Cy5.5 for 24 h and observed under a fluorescence microscope. The results confirmed that Cy5.5-Mitocelle penetrated deeply into the cartilage matrix and yielded a high signal intensity (Fig. 4A). To evaluate the stability and diffusion of Mitocelle in the cartilage matrix, Cy5.5-Mitocelle was injected intra-articularly, mouse joints were sampled at 24 h post-injection, and fluorescence images were analyzed. A higher intensity of Cy5.5 was observed in samples from mice injected with Cy5.5-Mitocelle compared to free Cy5.5 (Fig. 4B). To evaluate retention in the synovial membrane, Mitocelle was intra-articularly injected into mice and assessed at various time points under fluorescence microscopy. The fluorescence intensity of cartilage injected with free Cy5.5 decreased rapidly from 12 h, whereas cartilage injected with Cy5.5-Mitocelle maintained a strong fluorescence intensity up to 48 h post-injection and continued to exhibit fluorescence up to 168 h post-injection (Fig. 4C). Thus, the retention time of Cy5.5-Mitocelle in an injected joint was longer than that of free Cy5.5. Moreover, our organ distribution analysis showed that intra-articularly injected Mitocelle

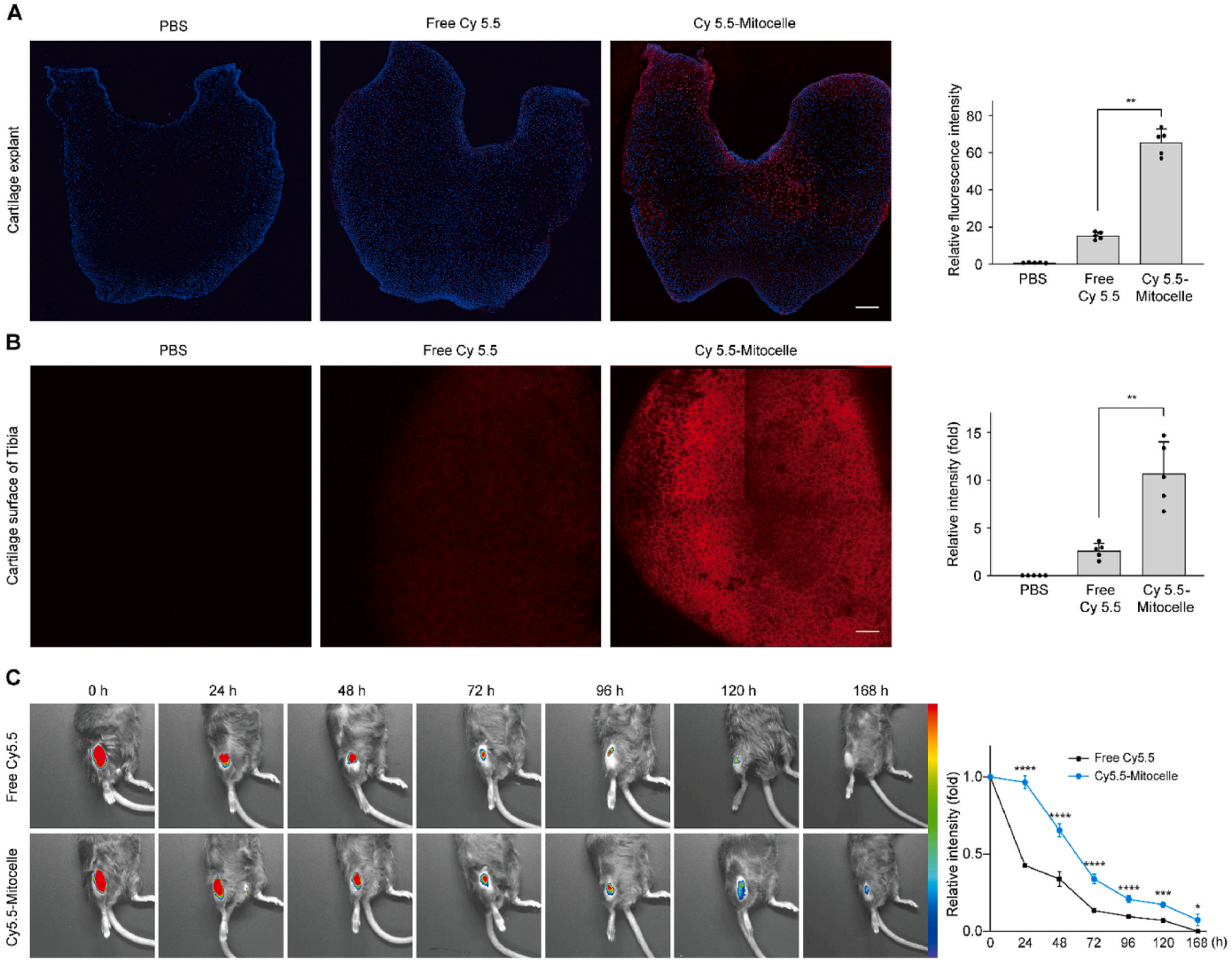

Fig. 4. Enhanced penetration and extended retention of Mitocelle in cartilage matrix. (A) Fluorescence microscopy images of mouse articular cartilage explants exposed to free Cy5.5 or Cy5.5-labeled Mitocelle for 24 h (left). Quantification of the fluorescence penetration depth (right). Scale bar, 100 μm. (B) Fluorescence microscopy images of mouse articular cartilage sampled at 24 h after intra-articular injection of Cy5.5-labeled Mitocelle (red). Scale bar, 20 μm. Quantification of the fluorescence intensity of Cy5.5 (right). (C) Retention time of free Cy5.5 and Cy5.5-labeled Mitocelle injected into the knee joints of C57BL/6 mice (left). Data are presented as means ± SD ($n = 5$) and were assessed using (A, B) Mann-Whitney *U* test or (C) one-way ANOVA with Bonferroni's test. $^{*}P < 0.05$, $^{**}P < 0.01$, $^{***}P < 0.001$, $^{****}P < 0.0001$.

showed no evidence of diffusing to another organ such as the heart, lung, liver, or spleen, and was ultimately excreted mainly via renal excretion up to 120 h post-injection (Fig. S9). We saw no evidence of synovial inflammation when Mitocelle was intra-articularly injected at 1-, 2-, or 4-week intervals after DMM surgery, nor did we observe inflammation of the lung, liver, or kidney under the most frequent dosing schedule (1-week intervals) (Fig. S10). Together, these results show that injected Mitocelle does not provoke toxicity in the synovium, lung, liver, or kidney, supporting its potential to be developed for clinical use as an inhibitor of OA development.

3.5. Therapeutic effects of Mitocelle under OA-mimicking conditions in vitro and in vivo

We next assessed the effect of Mitocelle on NOX4-induced OA-related catabolic factor expression. GSEA demonstrated that Mitocelle inhibited the NOX4-induced up-regulation of the OA gene signature (Fig. 5A). Analysis of collagenase, PGE_2, and ROS production revealed that Mitocelle treatment inhibited the NOX4-induced up-regulation of matrix degradation, inflammation, and ROS production (Fig. 5B, Figs. S11A and B). Additionally, the NOX4-induced up-regulation of the mRNA expression levels of OA-related catabolic factors was reversed by Mitocelle (Fig. S11C). In parallel experiments involving Mitocelle that had been stored for 2 weeks in solution or 1 year in the lyophilized state, we found no change in ability of Mitocelle to inhibit catabolic factor expression under the OA-mimicking condition *in vitro* (Fig. S12), indicating that the *in vitro* efficacy was maintained in Mitocelle that had undergone storage. We compared the antioxidant activities of Mitocelle with those of the vitamin A derivative, RP, which is well known to exert antioxidant activity and regulate catabolic factor expression [51,52]. Indeed, we found that, compared to RP, Mitocelle had greater efficacy in scavenging DPPH radical (Fig. S13A) and inhibiting catabolic activity (Fig. S13B). Thus, Mitocelle exhibited strong antioxidant activity and inhibition of catabolic factor expression under NOX4-induced OA-mimicking conditions *in vitro*, and such effects could be seen even after the preparation was stored for 1 year in a lyophilized state.

To examine the therapeutic effect of Mitocelle on OA development *in vivo*, we performed intra-articular injection of PBS and Mitocelle into DMM-induced OA model mice. We previously found that DMM-induced cartilage destruction is first detectable at 4 weeks after DMM surgery [34]. Therefore, Mitocelle was injected intra-articularly for 6 weeks at 1-week intervals starting at 4 weeks after DMM surgery (Fig. S14A). The degree of knee joint damage was scored using OARSI, osteophyte formation, and subchondral bone plate thickness analyses, which are used

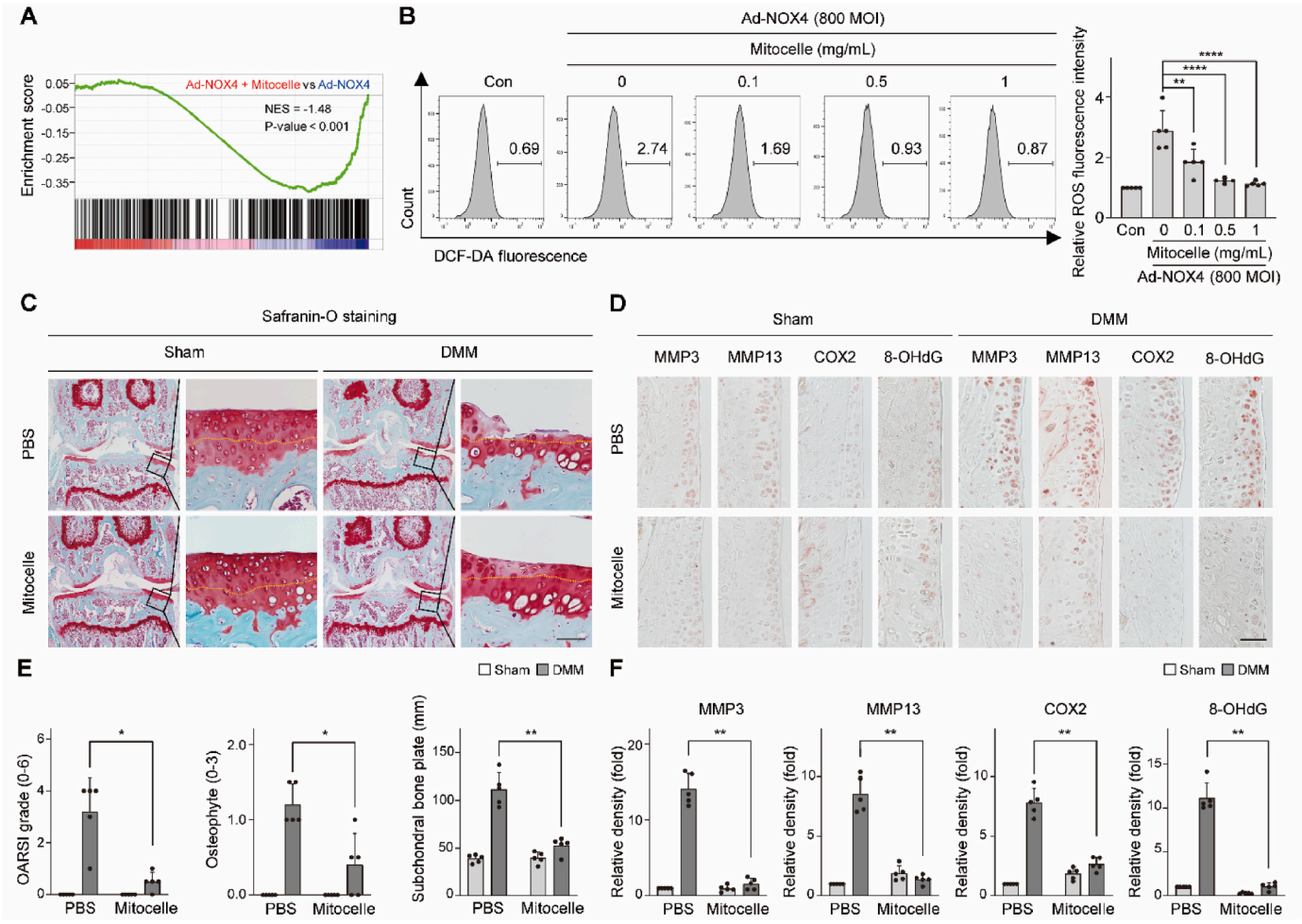

Fig. 5. Mitocelle alleviates cartilage destruction by downregulating ROS levels. (A) GSEA of Ad-NOX4-infected chondrocytes treated with or without Mitocelle. (B) Chondrocytes infected with Ad-NOX4 (800 MOI) were treated with Mitocelle, and intracellular ROS levels were assessed using DCF-DA. (C) Safranin-O staining and (D) immunohistochemical analysis examining the effect of Mitocelle in DMM-induced mice. After DMM surgery, intra-articular injection of Mitocelle was performed at 4-week intervals. Scale bar, 100 μm. (E) To evaluate the degree of cartilage damage, OARSI grade, osteophyte formation, and subchondral bone plate thickness were measured. (F) Relative densitometry assessing the expression levels of the OA-related catabolic factors, MMP3, MMP13, COX2, and 8-OHdG. Yellow dotted lines indicate tidemarks (C). Data are presented as means ± SD ($n = 5$) and were assessed using (B) one-way ANOVA with Bonferroni's test or (E, F) Mann-Whitney *U* test. $^{*}P < 0.05$, $^{**}P < 0.01$, $^{****}P < 0.0001$.

to grade OA. Our results showed that this intra-articular injection of Mitocelle significantly reduced the degree of cartilage damage (Figs. S14C and E) and the expression levels of OA catabolic factors and the ROS marker, 8-OHdG (Fig. S14G). Knee injections may provide only temporary relief, so patients should be prepared to find other ways to manage their knee pain in the long run [53]. Although our results suggest that Mitocelle has no cytotoxicity and is taken into cartilage *in vitro*, *in vivo*, and *ex vivo*, the duration of its efficacy remains unclear. That said, we found that Mitocelle was sufficiently effective in our experimental setting when administered at intervals of 2 weeks (Figs. S14B, D, F, H) or 4 weeks (Fig. 5C–F). Our findings confirm that Mitocelle effectively prevents the breakdown of osteoarthritic cartilage by inhibiting the expression of OA-related catabolic factors, thereby reducing the symptoms of OA. Together, our results show that Mitocelle, which is composed of FDA-approved biocompatible materials, can effectively reduce the levels of cartilage-damaging factors and inhibit OA-related catabolic factor expression without cytotoxicity to exert long-lasting effects that may minimize the extent of osteoarthritic cartilage destruction. Therefore, injecting Mitocelle directly into the joint could be a promising approach for treating OA.

3.6. Molecular mechanism through which Mitocelle decreases catabolic factor expression

Lastly, we investigated the mechanism through which the Mitocelle/NOX4 interaction inhibits the ability of NOX4 to increase catabolic factor expression. p22phox is an essential component of the NADPH oxidase complex, and the NOX4-p22phox interaction is primarily responsible for generating ROS [14,15,54]. We found that p22phox appeared on the list of Mitocelle-altered genes involved in ROS generation (Fig. 6A and B), suggesting that Mitocelle competitively inhibits the NOX4-p22phox complex. To test this hypothesis, we performed FRET analysis, particularly looking at acceptor photobleaching (Fig. 6C). We used the FRET signal for the positive-control fusion protein to establish the experimental conditions (Fig. S15). We then co-transfected NOX4-YFP and p22phox-CFP and examined whether there was direct binding between NOX4 and p22phox. Indeed, we observed that the signal intensity of p22phox-CFP (donor) increased when NOX4-YFP (acceptor) was bleached in a specific region. However, Mitocelle treatment either decreased or failed to change the donor intensity (Fig. 6D). Our calculation of FRET efficiency showed that the Mitocelle-treated group showed a significant decrease (Fig. 6E). Thus, NOX4 and p22phox generated significant FRET signals under control conditions but not under Mitocelle treatment. These findings suggest that, in the dysfunctional mitochondria of chondrocytes present in OA conditions, Mitocelle interferes with the formation of the NOX4-p22phox complex to inhibit NOX4-induced ROS generation and downstream OA-related catabolic factor expression.

4. Discussion

Mitochondrial dysfunction is a key factor in numerous cellular organelle disorders; it impacts multiple facets of cellular well-being and operation due to the pivotal involvement of mitochondria in energy generation, apoptosis (controlled cell death), and metabolic pathways [55]. Malfunction of mitochondria can have a domino effect on other organelles and cellular systems to worsen or intensify pathological conditions [2]. Accumulating evidence indicates that mitochondrial dysfunction plays an important role in the development of OA, which is a degenerative joint disease defined by the deterioration of joint cartilage and underlying bone [56]. Mitochondrial dysfunction in joint tissues, especially in cartilage-maintaining chondrocytes, is a major contributor to the development and progression of OA. This dysfunction is influenced by biochemical, mechanical, and environmental factors [57]. Biocompatible materials capable of scavenging ROS are expected to have tremendous therapeutic potential in treating OA. However, they are currently limited in terms of their selectivity, specificity, biocompatibility, targeted administration, and regulatory approval.

In this study, we developed Mitocelle as a novel nano-formulation that effectively addresses many of the limitations of earlier approaches, and propose it as a safe and dependable pharmaceutical option. To develop Mitocelle, we utilized biocompatible povidone as a template polymer to enhance the stability of PB. Povidone creates complexes with medications and other compounds to enhance their stability and solubility. PB is employed in medicine as an antidote for heavy metal poisoning with thallium or radioactive cesium. We developed a quick and efficient procedure for synthesizing Mitocelle without any requirement for heat or a reducing agent. As prepared, Mitocelle exhibited distinctive attributes and enhanced resistance to clumping, compared to PB alone, which quickly formed solid particles when maintained in a biological buffer. The component materials have already been approved by the US FDA, and our results suggest that they do not cause any harm to chondrocytes or other organs.

Our experiments showed that Mitocelle moves from the cartilage matrix to the cytoplasm of chondrocytes, where it specifically targets and identifies malfunctioning mitochondria. Mechanistically, mitochondrial dysfunction is connected to OA via the NOX4-p22phox axis-governed overproduction of ROS, which triggers OA-related catabolic factor expression. Mitocelle is one of nanoparticles, it could bind to a protein through shape and size compatibility [38]. The physical dimensions of Mitocelle may be tailored to fit the pocket of NOX4 formed by p22phox interaction, potentially blocking or altering the active site or another functional region of the enzyme. Consistent with this, our results demonstrated that inhibition of NOX4 leads to decreases OA-related changes. Here, we report that Mitocelle binds to NOX4 and p22phox and disrupts their complexation to inhibit NOX4 activity, and thereby reduces ROS generation and alleviates the oxidative stress-related development of OA.

We further reveal that the localized intra-articular knee injection of Mitocelle is highly beneficial for the treatment of OA, without showing any organ cytotoxicity in a mouse model. Although OA leads to inflammation, cartilage degradation, and bone structure alterations, the current intra-articular injection-based therapies mostly focus on suppressing inflammation and improving knee mobility through the use of corticosteroids and HA. Here, we found that OA model mice given knee-joint injections of Mitocelle at intervals of 1, 2, or 4 weeks after the commencement of OA development demonstrated suppression of catabolic factor expression and OA symptoms. Cy5.5-Mitocelle was retained in an injected joint for longer than free Cy5.5 without showing evidence of diffusion to another organ, and was excreted mainly via renal excretion. Mitocelle comprises biocompatible materials that are very stable to degradation and can inhibit the expression of catabolic factors triggered by the NOX4-p22phox interaction. The retention time of hydrogels in the knee joint is crucial for their effectiveness, especially in therapeutic applications such as delivering drugs or aiding in tissue repair. Interestingly, gallic acid-grafted gelatin hydrogel (GLP hydrogel) has the capacity to release liposome-anchored teriparatide into a knee joint [58]. The utilization of gelatin hydrogel also facilitates the prolonged and controlled delivery of antioxidant PGA-Mn nanoparticles within the joint [59]. Therefore, to improve the retention time of Mitocelle in cartilage, it might prove useful to add GLP, or other functional hydrogels.

In sum, we herein show that our newly developed formulation, Mitocelle, addresses some of the constraints and obstacles associated with inhibiting defective mitochondria, such as problems with selectivity, delivery, unknown molecular mechanisms, and toxicity. Our research indicates that Mitocelle shows promise as a safe and easily translatable medication for treating OA and other NOX4-related cellular organelle disorders. In the future, it is plausible that Mitocelle may also be employed as a delivery agent for transporting drugs to malfunctioning mitochondria in other conditions.

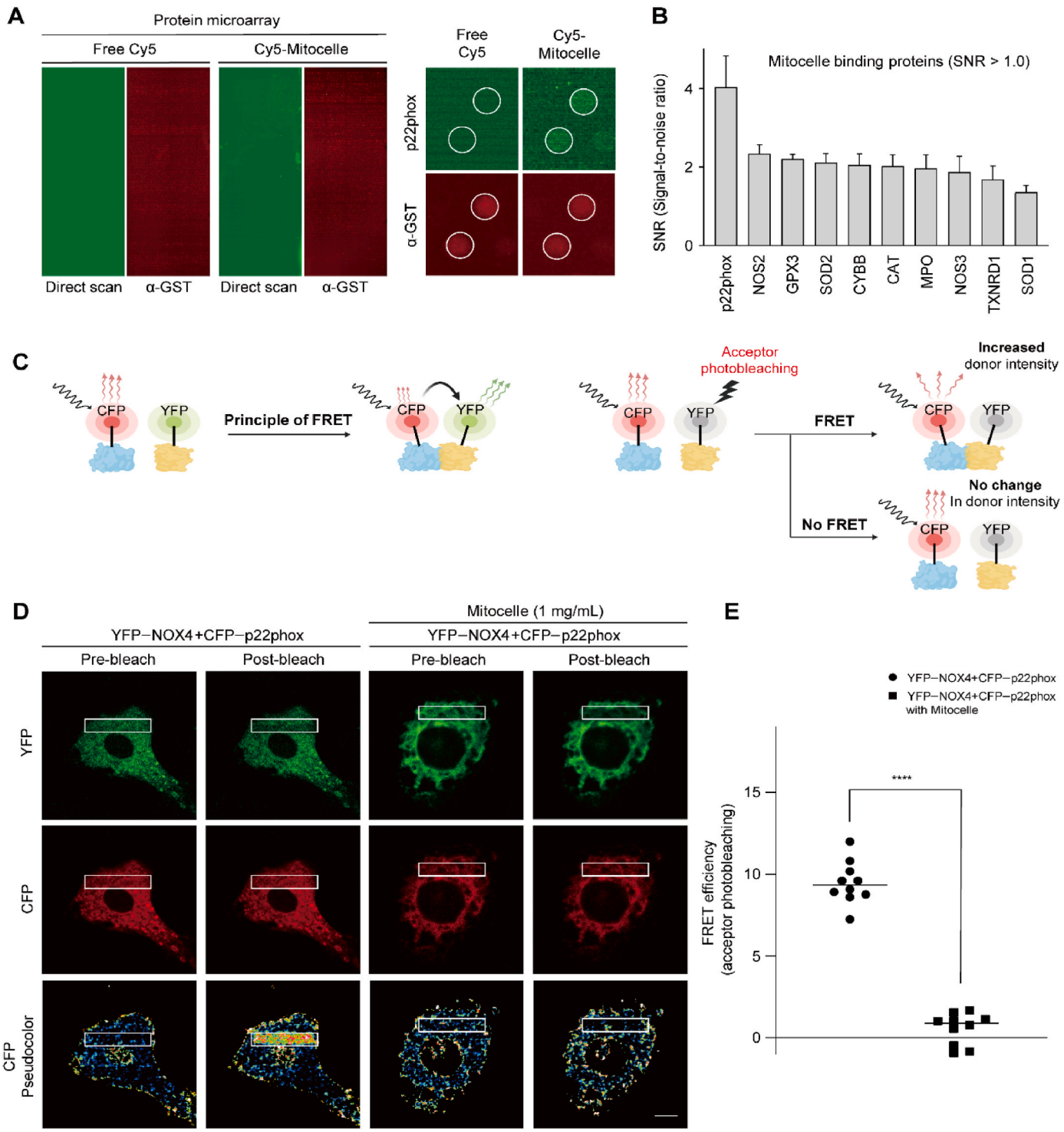

Fig. 6. Mitocelle interferes with the NOX4-p22phox interaction that contributes to ROS generation. (A) HuProt™ 3.1 Human Protein chip was used to analyze the effects of free Cy5 and Cy5-labeled Mitocelle (5 μg/mL) on Mitocelle-interacting proteins. The signal-to-noise ratio (SNR) of each point was calculated as the ratio of foreground to background signal. Additionally, a high-power image of p22phox binding (white circle) is shown in the right panel. (B) The SNR >1.0 proteins included 10 proteins known to be involved in ROS generation. (C) Schematic illustration of the principle of FRET and the acceptor photobleaching used for FRET measurements; CFP (donor), YFP (acceptor). (D) FRET detection by acceptor photobleaching. Chondrocytes were transfected for 24 h with vectors encoding YFP-NOX4 and CFP-p22phox, Mitocelles were applied, and transfection was continued for an additional 24 h. Fluorescence images were collected using YFP and CFP channels before and after photobleaching. To better show the changes in CFP fluorescence, pre- and post-bleaching CFP images are presented using pseudocolor. (E) FRET efficiency was measured after acceptor bleaching. Data are presented as means ± SD ($n = 10$) and were assessed using (E) Mann-Whitney U test. ****$P < 0.0001$.

5. Conclusion

We herein describe the development of an intra-articularly injectable Mitocelle by coating ROS-scavenging PB with biocompatible povidone, show that it decreases the severity of OA in a mouse model, and accordingly suggest Mitocelle as a new treatment strategy for OA. NOX4-p22phox axis-induced ROS production is well balanced in normal mitochondria. When this balance is disrupted by a pathogenic factor, ROS production increases to cause mitochondrial dysfunction. Here, our protein array and FRET analyses demonstrate that Mitocelle directly interferes with the interaction between NOX4 and p22phox to inhibit ROS production, alleviate mitochondrial dysfunction, and downregulate OA-related catabolic factors. To our knowledge, this is the first paper to show that regulating ROS production by interfering with the NOX4-p22phox interaction in chondrocytes can have therapeutic effects in OA. Therefore, we strongly suggest that Mitocelle holds promise as a possible treatment for OA and, potentially, for other pathologies that show similar underlying patterns of mitochondrial damage.

Ethics approval and consent to participate

Human OA cartilage was sourced from patients who underwent arthroplasty (Table S1). All patients provided written informed consent, and the collection was approved by the Institutional Review Board of the Catholic University of Korea (UC14CNSI0150). The undamaged portion of cartilage from human OA patients was defined as healthy cartilage. All animal experiments were approved by the Animal Care and Use Committee of Sungkyunkwan University (protocol code SKKUIA-CUC2023-07-17-1).

Data availability

The data used to support the findings of this study have been included in this article.

CRediT authorship contribution statement

Min Ju Lim: Writing – original draft, Visualization, Validation, Methodology, Investigation, Formal analysis. **Hyeryeon Oh:** Writing – original draft, Validation, Methodology, Investigation, Formal analysis, Conceptualization. **Jimin Jeon:** Methodology, Formal analysis. **Chanmi Cho:** Methodology, Formal analysis, Conceptualization. **Jin Sil Lee:** Validation, Resources, Formal analysis. **Yiseul Hwang:** Validation, Investigation, Formal analysis. **Seok Jung Kim:** Resources, Investigation, Formal analysis. **Jung-Soon Mo:** Validation, Investigation, Data curation. **Panmo Son:** Validation, Formal analysis. **Ho Chul Kang:** Writing – review & editing, Writing – original draft, Supervision, Project administration, Funding acquisition, Conceptualization. **Won Il Choi:** Writing – review & editing, Writing – original draft, Validation, Supervision, Project administration, Funding acquisition, Data curation, Conceptualization. **Siyoung Yang:** Writing – review & editing, Writing – original draft, Supervision, Project administration, Funding acquisition, Data curation, Conceptualization.

Declaration of competing interest

The authors declare that they have no known competing financial interests or personal relationships that could have appeared to influence the work reported in this paper.

Acknowledgments

This work was supported by the National Research Foundation, funded by the Ministry of Science & ICT (2021M3C1C3097647, NRF-2022R1A2C2004343, RS-2023-00223552, and RS-2024-00335111), the Korea Healthcare Technology R&D project of the Korea Health Industry Development Institute (HI16C0001 and HR22C1734), a Korean Fund for Regenerative Medicine (KFRM) grant funded by the Korea government (the Ministry of Science and ICT, the Ministry of Health & Welfare, 23C0113L1), and the Korea Institute of Ceramic Engineering and Technology (KICET, 2410002182).

Appendix A. Supplementary data

Supplementary data to this article can be found online at https://doi.org/10.1016/j.bioactmat.2024.09.021.

References

[1] J.S. Harrington, S.W. Ryter, M. Plataki, et al., Mitochondria in health, disease, and ageing, Physiol. Rev. (2023), https://doi.org/10.1152/physrev.00058.2021.
[2] K. Shen, C.L. Pender, R. Bar-Ziv, et al., Mitochondria as cellular and organismal signaling hubs, Annu. Rev. Cell Dev. Biol. 38 (2022) 179–218, https://doi.org/10.1146/annurev-cellbio-120420-015303.
[3] X. Liu, M. Li, Z. Chen, et al., Mitochondrial calpain-1 activates NLRP3 inflammasome by cleaving ATP5A1 and inducing mitochondrial ROS in CVB3-induced myocarditis, Basic Res. Cardiol. 117 (2022) 40, https://doi.org/10.1007/s00395-022-00948-1.
[4] P. Sulkshane, J. Ram, A. Thakur, et al., Ubiquitination and receptor-mediated mitophagy converge to eliminate oxidation-damaged mitochondria during hypoxia, Redox Biol. 45 (2021) 102047, https://doi.org/10.1016/j.redox.2021.102047.
[5] J.A. Amorim, G. Coppotelli, A.P. Rolo, et al., Mitochondrial and metabolic dysfunction in ageing and age-related diseases, Nat. Rev. Endocrinol. 18 (2022) 243–258, https://doi.org/10.1038/s41574-021-00626-7.
[6] K.H. Cleveland, R.G. Schnellmann, Pharmacological targeting of mitochondria in diabetic kidney disease, Pharmacol. Rev. 75 (2023) 250–262, https://doi.org/10.1124/pharmrev.122.000560.
[7] D.N. Jackson, A.L. Theiss, Gut bacteria signaling to mitochondria in intestinal inflammation and cancer, Gut Microb. 11 (2020) 285–304, https://doi.org/10.1080/19490976.2019.1592421.
[8] M.A. Eldeeb, R.A. Thomas, M.A. Ragheb, et al., Mitochondrial quality control in health and in Parkinson's disease, Physiol. Rev. 102 (2022) 1721–1755, https://doi.org/10.1152/physrev.00041.2021.
[9] K. Sun, X. Jing, J. Guo, et al., Mitophagy in degenerative joint diseases, Autophagy 17 (2021) 2082–2092, https://doi.org/10.1080/15548627.2020.1822097.
[10] Z. Jiang, H. Wang, Z. Zhang, et al., Cartilage targeting therapy with reactive oxygen species-responsive nanocarrier for osteoarthritis, J. Nanobiotechnol. 20 (2022) 419, https://doi.org/10.1186/s12951-022-01629-w.
[11] M. Tu, M. Yang, N. Yu, et al., Inhibition of cyclooxygenase-2 activity in subchondral bone modifies a subtype of osteoarthritis, Bone Res 7 (2019) 29, https://doi.org/10.1038/s41413-019-0071-x.
[12] L.J. Kang, J. Yoon, J.G. Rho, et al., Self-assembled hyaluronic acid nanoparticles for osteoarthritis treatment, Biomaterials 275 (2021) 120967, https://doi.org/10.1016/j.biomaterials.2021.120967.
[13] R. Begum, S. Thota, A. Abdulkadir, et al., NADPH oxidase family proteins: signaling dynamics to disease management, Cell. Mol. Immunol. 19 (2022) 660–686, https://doi.org/10.1038/s41423-022-00858-1.
[14] S. O'Neill, U.G. Knaus, Protein-protein interaction assay to analyze NOX4/p22 (phox) heterodimerization, Methods Mol. Biol. 1982 (2019) 447–458, https://doi.org/10.1007/978-1-4939-9424-3_26.
[15] J. Sun, J. Chen, T. Li, et al., ROS production and mitochondrial dysfunction driven by PU. 1-regulated NOX4-p22phox activation in Aβ-induced retinal pigment epithelial cell injury, Theranostics 10 (2020) 11637, https://doi.org/10.7150/thno.48064.
[16] C. Michaeloudes, H. Abubakar-Waziri, R. Lakhdar, et al., Molecular mechanisms of oxidative stress in asthma, Mol. Aspect. Med. 85 (2022) 101026, https://doi.org/10.1016/j.mam.2021.101026.
[17] X. Fan, T. Dong, K. Yan, et al., PM2.5 increases susceptibility to acute exacerbation of COPD via NOX4/Nrf2 redox imbalance-mediated mitophagy, Redox Biol. 59 (2023) 102587, https://doi.org/10.1016/j.redox.2022.102587.
[18] J. Jeon, H. Lee, M.S. Jeon, et al., Blockade of activin receptor IIB protects arthritis pathogenesis by non-amplification of activin A-ACVR2B-NOX4 Axis pathway, Adv. Sci. 10 (2023) e2205161, https://doi.org/10.1002/advs.202205161.
[19] M. Arra, G. Swarnkar, K. Ke, et al., LDHA-mediated ROS generation in chondrocytes is a potential therapeutic target for osteoarthritis, Nat. Commun. 11 (2020) 3427, https://doi.org/10.1038/s41467-020-17242-0.
[20] W. Hou, C. Ye, M. Chen, et al., Excavating bioactivities of nanozyme to remodel microenvironment for protecting chondrocytes and delaying osteoarthritis, Bioact. Mater. 6 (2021) 2439–2451, https://doi.org/10.1016/j.bioactmat.2021.01.016.
[21] T. Zhou, J. Ran, P. Xu, et al., A hyaluronic acid/platelet-rich plasma hydrogel containing MnO2 nanozymes efficiently alleviates osteoarthritis in vivo, Carbohydr. Polym. 292 (2022) 119667, https://doi.org/10.1016/j.carbpol.2022.119667.
[22] M.S. Lord, J.F. Berret, S. Singh, et al., Redox active cerium oxide nanoparticles: current status and burning issues, Small 17 (2021) e2102342, https://doi.org/10.1002/smll.202102342.

[23] X. Wang, L. Cheng, Multifunctional Prussian blue-based nanomaterials: preparation, modification, and theranostic applications, Coord. Chem. Rev. 419 (2020) 213393, https://doi.org/10.1016/j.ccr.2020.213393.
[24] G. Zhong, H. Long, T. Zhou, et al., Blood-brain barrier Permeable nanoparticles for Alzheimer's disease treatment by selective mitophagy of microglia, Biomaterials 288 (2022) 121690, https://doi.org/10.1016/j.biomaterials.2022.121690.
[25] X. Xie, J. Zhao, W. Gao, et al., Prussian blue nanozyme-mediated nanoscavenger ameliorates acute pancreatitis via inhibiting TLRs/NF-κB signaling pathway, Theranostics 11 (2021) 3213, https://doi.org/10.7150/thno.52010.
[26] K. Zhang, M. Tu, W. Gao, et al., Hollow prussian blue nanozymes drive neuroprotection against ischemic stroke via attenuating oxidative stress, counteracting inflammation, and suppressing cell apoptosis, Nano Lett. 19 (2019) 2812–2823, https://doi.org/10.1021/acs.nanolett.8b04729.
[27] Z. Qin, B. Chen, Y. Mao, et al., Achieving ultrasmall Prussian blue nanoparticles as high-performance biomedical agents with multifunctions, ACS Appl. Mater. Interfaces 12 (2020) 57382–57390, https://doi.org/10.1021/acsami.0c18357.
[28] W. Wu, L. Yu, Y. Pu, et al., Copper-enriched prussian blue nanomedicine for in situ disulfiram toxification and photothermal antitumor amplification, Adv. Mater. 32 (2020) e2000542, https://doi.org/10.1002/adma.202000542.
[29] X. Ma, J. Hao, J. Wu, et al., Prussian blue nanozyme as a pyroptosis inhibitor alleviates neurodegeneration, Adv. Mater. 34 (2022) e2106723, https://doi.org/10.1002/adma.202106723.
[30] T. Uemura, S. Kitagawa, Prussian blue nanoparticles protected by poly (vinylpyrrolidone), J. Am. Chem. Soc. 125 (2003) 7814–7815, https://doi.org/10.1021/ja0356582.
[31] H. Zhang, S. Nakamura, D.D. Kitts, Antioxidant properties of casein phosphopeptides (CPP) and maillard-type conjugated products, Antioxidants 9 (2020), https://doi.org/10.3390/antiox9080648.
[32] A. Sentkowska, K. Pyrzynska, The influence of synthesis conditions on the antioxidant activity of selenium nanoparticles, Molecules 27 (2022), https://doi.org/10.3390/molecules27082486.
[33] S. Yang, J. Kim, J.-H. Ryu, et al., Hypoxia-inducible factor-2α is a catabolic regulator of osteoarthritic cartilage destruction, Nat. Med. 16 (2010) 687–693, https://doi.org/10.1038/nm.2153.
[34] J. Jeon, H.J. Noh, H. Lee, et al., TRIM24-RIP3 axis perturbation accelerates osteoarthritis pathogenesis, Ann. Rheum. Dis. 79 (2020) 1635–1643, https://doi.org/10.1136/annrheumdis-2020-217904.
[35] R.K. Ambasta, P. Kumar, K.K. Griendling, et al., Direct interaction of the novel Nox proteins with p22phox is required for the formation of a functionally active NADPH oxidase, J. Biol. Chem. 279 (2004) 45935–45941, https://doi.org/10.1074/jbc.M406486200.
[36] J. Geng, Y. Shi, J. Zhang, et al., TLR4 signalling via Piezo1 engages and enhances the macrophage mediated host response during bacterial infection, Nat. Commun. 12 (2021) 3519, https://doi.org/10.1038/s41467-021-23683-y.
[37] R.D. Maynard, D.A. Villani, W.G. Schroeder, et al., Surgical induction of posttraumatic osteoarthritis in the mouse, Methods Mol. Biol. 2230 (2021) 91–103, https://doi.org/10.1007/978-1-0716-1028-2_6.
[38] C. Cho, J.S. Lee, H. Oh, et al., Fructose-derived levan nanoparticles protect against osteoarthritis by directly blocking CD44 activation, Small 18 (2022) 2202146, https://doi.org/10.1002/smll.202202146.
[39] H.J. Maeng, D.-H. Kim, N.-W. Kim, et al., Synthesis of spherical Prussian blue with high surface area using acid etching, Curr. Appl. Phys. 18 (2018) S21–S27, https://doi.org/10.1016/j.cap.2017.11.014.
[40] H. Buser, D. Schwarzenbach, W. Petter, et al., The crystal structure of Prussian blue: Fe4 [Fe (CN) 6] 3. xH2O, Inorg. Chem. 16 (1977) 2704–2710, https://doi.org/10.1021/ic50177a008.
[41] W. Zhang, S. Hu, J.J. Yin, et al., Prussian blue nanoparticles as multienzyme mimetics and reactive oxygen species scavengers, J. Am. Chem. Soc. 138 (2016) 5860–5865, https://doi.org/10.1021/jacs.5b12070.
[42] K. Todkar, L. Chikhi, M. Germain, Mitochondrial interaction with the endosomal compartment in endocytosis and mitochondrial transfer, Mitochondrion 49 (2019) 284–288, https://doi.org/10.1016/j.mito.2019.05.003.
[43] L. Simón, A. Campos, L. Leyton, et al., Caveolin-1 function at the plasma membrane and in intracellular compartments in cancer, Cancer Metastasis Rev. 39 (2020) 435–453, https://doi.org/10.1007/s10555-020-09890-x.
[44] F. Guerra, C. Bucci, Multiple roles of the small GTPase Rab7, Cells 5 (2016), https://doi.org/10.3390/cells5030034.
[45] Y. Jiang, S. Krantz, X. Qin, et al., Caveolin-1 controls mitochondrial damage and ROS production by regulating fission - fusion dynamics and mitophagy, Redox Biol. 52 (2022) 102304, https://doi.org/10.1016/j.redox.2022.102304.
[46] M.S. Deffieu, I. Cesonyte, F. Delalande, et al., Rab7-harboring vesicles are carriers of the transferrin receptor through the biosynthetic secretory pathway, Sci. Adv. 7 (2021), https://doi.org/10.1126/sciadv.aba7803.
[47] A. Das, S. Nag, A.B. Mason, et al., Endosome-mitochondria interactions are modulated by iron release from transferrin, J. Cell Biol. 214 (2016) 831–845, https://doi.org/10.1083/jcb.201602069.
[48] J. Li, L. Wang, B. Wang, et al., NOX4 is a potential therapeutic target in septic acute kidney injury by inhibiting mitochondrial dysfunction and inflammation, Theranostics 13 (2023) 2863–2878, https://doi.org/10.7150/thno.81240.
[49] W. Wang, J. Duan, W. Ma, et al., Trimanganese tetroxide nanozyme protects cartilage against degeneration by reducing oxidative stress in osteoarthritis, Adv. Sci. 10 (2023) e2205859, https://doi.org/10.1002/advs.202205859.
[50] Z. Yu, Z. Xiao, L. Guan, et al., Translocation of gasdermin D induced mitochondrial injury and mitophagy mediated quality control in lipopolysaccharide related cardiomyocyte injury, Clin. Transl. Med. 12 (2022) e1002, https://doi.org/10.1002/ctm2.1002.
[51] H. Oh, J.S. Lee, S. Kim, et al., Super-antioxidant vitamin A derivatives with improved stability and efficacy using skin-permeable chitosan nanocapsules, Antioxidants 12 (2023), https://doi.org/10.3390/antiox12111913.
[52] E. Souganidis, A. Laillou, M. Leyvraz, et al., A comparison of retinyl palmitate and red palm oil β-carotene as strategies to address Vitamin A deficiency, Nutrients 5 (2013) 3257–3271, https://doi.org/10.3390/nu5083257.
[53] I.A. Jones, R. Togashi, M.L. Wilson, et al., Intra-articular treatment options for knee osteoarthritis, Nat. Rev. Rheumatol. 15 (2019) 77–90, https://doi.org/10.1038/s41584-018-0123-4.
[54] K.K. Prior, M.S. Leisegang, I. Josipovic, et al., CRISPR/Cas9-mediated knockout of p22phox leads to loss of Nox1 and Nox4, but not Nox5 activity, Redox Biol. 9 (2016) 287–295, https://doi.org/10.1016/j.redox.2016.08.013.
[55] L. Mei, X. Chen, F. Wei, et al., Tethering ATG16L1 or LC3 induces targeted autophagic degradation of protein aggregates and mitochondria, Autophagy 19 (2023) 2997–3013, https://doi.org/10.1080/15548627.2023.2234797.
[56] L. Zheng, Z. Zhang, P. Sheng, et al., The role of metabolism in chondrocyte dysfunction and the progression of osteoarthritis, Ageing Res. Rev. 66 (2021) 101249, https://doi.org/10.1016/j.arr.2020.101249.
[57] W. Jiang, H. Liu, R. Wan, et al., Mechanisms linking mitochondrial mechanotransduction and chondrocyte biology in the pathogenesis of osteoarthritis, Ageing Res. Rev. 67 (2021) 101315, https://doi.org/10.1016/j.arr.2021.101315.
[58] G. Li, S. Liu, Y. Chen, et al., An injectable liposome-anchored teriparatide incorporated gallic acid-grafted gelatin hydrogel for osteoarthritis treatment, Nat. Commun. 14 (2023) 3159, https://doi.org/10.1038/s41467-023-38597-0.
[59] Q. Chen, Y. Jin, T. Chen, et al., Injectable nanocomposite hydrogels with enhanced lubrication and antioxidant properties for the treatment of osteoarthritis, Mater Today Bio 25 (2024) 100993, https://doi.org/10.1016/j.mtbio.2024.100993.